Superior performance of highly flexible solid-state supercapacitor based on the ternary composites of graphene oxide supported poly(3,4-ethylenedioxythiophene)-carbon nanotubes

Haihan Zhou[*], Hua-Jin Zhai, Gaoyi Han

Institute of Molecular Science, Key Laboratory of Materials for Energy Conversion and Storage of Shanxi Province, Key Laboratory of Chemical Biology and Molecular Engineering of Education Ministry, Shanxi University, Taiyuan 030006, China

HIGHLIGHTS

- GO/PEDOT-CNTs ternary composites are prepared via a facile electrochemical method.
- The long CNTs more effectively improve the capacitive performance of GO/PEDOT.
- A lightweight and thin solid-state highly flexible supercapacitor is fabricated.
- The supercapacitor device shows a high specific capacitance and cycle stability.

GRAPHICAL ABSTRACT
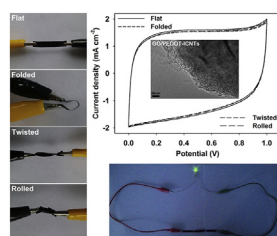
ABSTRACT

Ternary composite electrodes based on carbon nanotubes thin films (CNFs)-loaded graphene oxide (GO) supported poly(3,4-ethylenedioxythiophene)- carbon nanotubes (GO/PEDOT-CNTs) have been prepared via a facile one-step electrochemical codeposition method. The effect of long and short CNTs-incorporated composites (GO/PEDOT-lCNTs and GO/PEDOT-sCNTs) on the electrochemical behaviors of the electrodes is investigated and compared. Electrochemical measurements indicate that the incorporation of CNTs effectively improves the electrochemical performances of the GO/PEDOT electrodes. Long CNTs-incorporated GO/PEDOT-lCNTs electrodes have more superior electrochemical behaviors with respect to the short CNTs-incorporated GO/PEDOT-lCNTs electrodes, which can be attributed to the optimized composition and specific microstructures of the former. To verify the feasibility of the prepared composite electrodes for utilization as flexible supercapacitor, a solid-state supercapacitor using the CNFs-loaded GO/PEDOT-lCNTs electrodes is fabricated and tested. The device shows lightweight, ultrathin, and highly flexible features, which also has a high areal and volumetric specific capacitance ($33.4 \ \mathrm{m \ F \ cm^{-2}}$ at $10 \ \mathrm{mV \ s^{-1}}$ and $2.7 \ \mathrm{F \ cm^{-3}}$ at $0.042 \ \mathrm{A \ cm^{-3}}$), superior rate capability, and excellent cycle stability (maintaining 97.5% for 5000 cycles). This highly flexible solid-state supercapacitor has great potential for applications in flexible electronics, roll-up display, and wearable devices.

© 2016 Elsevier B.V. All rights reserved.

1. Introduction

Developing highly flexible energy storage devices with superior performance can meet the requirement for flexible electronics of

the next generation, which has potential technological applications in various fields, including but not limited to roll-up displays, artificial electronic skin, and wearable devices. For personal electronics and modern market, such devices follow the trend toward lightweight, thinness, miniaturization, and flexibility, and may be even rolled up [1—6]. Supercapacitors (also called electrochemical capacitors) are the promising candidates for flexible devices, due to their advantages including inherent electrochemical properties (high power density, rapid charge-discharge performance, and long-term cycle stability), relatively simple structures, as well as the easy production on large scale [7—10].

Commonly, supercapacitors can be divided into two categories based on the energy storage mechanism. One is the electrochemical double-layer capacitors (EDLCs), which usually use carbon materials with high power density as the accumulation of pure electrostatic charges in the electric double layers. The other is the Faradaic pseudocapacitors that employ conducting polymers and transition metal oxides/hydroxides, whose high energy density derives from the surface or near-surface redox reactions of electroactive species [11—14]. The electrode materials are crucial to the performance of supercapacitors. However, each electrode material has its advantages and disadvantages. For instance, carbon materials show high power density and long cycle stability, but they have low capacitance. Transition metal oxides exhibit higher energy density than carbon materials and a better cycle life than conducting polymers, but they also present a drawback of poor conductivity. Conducting polymers have high energy density, and yet they reveal the disadvantages of a low cycle life because swelling and shrinkage occur during the doping/dedoping of counter-ions [15—17]. Therefore, extensive attempts have been made to prepare composite electrode materials that can compensate for the limitation of each individual material used for supercapacitors. For instance, the hierarchical NiMn layered double hydroxide/carbon nanotubes [18], three dimensional (3D) carbon-metal oxide composite [19], and carbon@MnO_2 core-shell hybrid nanospheres [20], and so on.

Graphene oxide (GO) can be easily synthesized from natural graphite and forms stable dispersions in water. It has a low fabrication cost and is environmentally friendly in nature. GO also exhibits a high specific surface area that results in the large electrical double-layer. On the other hand, conducting polymers (CPs) have high Faradaic pseudocapacitance. Thus, a number of recent studies have been devoted to synthesizing the composites of CPs and GO nanosheets in order to achieve the large specific capacitance and long cycle life for electrochemical capacitors. Cao et al. reported the 3D GO/polypyrrole (GO/PPy) composite electrodes by electrochemical deposition [21]; Wu et al. demonstrated a facile and effective synthesis of GO/CPs (CPs, PANI and PPy) composites via an in situ oxidative polymerization [22]; Li et al. investigated the GO/PPy nanowire composite material using an in situ chemical polymerization method [23]; and Li et al. prepared the GO/PANI composites using an in-situ polymerized method [24]. In our previous study, the PPy/GO composites have been also investigated through an electrochemical codeposition method [25].

Although the above GO/CPs composites exhibit good capacitive performances due to the hydrophilic nature of GO and the $\pi-\pi$ stacking between GO layers and polymer rings, the GO still hinders their charge storage properties as a result of the insulating nature of GO (conductivity of 1.28×10^{-9} S cm^{-1}), which is caused by a large number of oxygen containing functional groups in its structure [21]. Carbon nanotubes (CNTs), owing to their high conductivity, low specific weight, ideal specific surface area and chemical stability, have been widely used as the supercapacitor electrode materials [26—28]. So incorporating CNTs into the GO/CPs composites has the potential to improve their electrochemical behaviors. Poly(3,4-ethylenedioxythiophene) (PEDOT) as an electrode material for supercapacitors has been extensively investigated. It exhibits not only a high conductivity, but also an unusual stability in the oxidized state as compared to other CPs [29,30]. In this contribution, we shall devote our effort to improving the electrochemical performances of the GO/PEDOT composites by incorporating the CNTs. The ternary GO/PEDOT-CNTs composites are readily prepared via a facile one-step electrochemical codeposition method. To our knowledge, no prior research has been made to prepare the ternary composites consisting of CPs, GO and CNTs for supercapacitor applications. Furthermore, we will investigate the effect of two types of CNTs (long versus short) on improving the electrochemical behaviors of the GO/PEDOT composites.

Carbon nanotube films (CNFs) are one kind of favorable substrate for flexible electric devices due to its superior flexibility, excellent electrical conductivity, and mechanical strength [31]. In this study, CNFs are used as the electrode substrate (mechanical support) as well as current collector to obtain a highly flexible, ultrathin, and lightweight electrode architecture. The CNFs-loaded long and short CNTs incorporated GO/PEDOT ternary composite electrodes (GO/PEDOT-lCNTs and GO/PEDOT-sCNTs) are prepared via a facile one-step electrochemical codeposition method. Their electrochemical behaviors were investigated and compared using the cyclic voltammetry (CV), galvanostatic charge/discharge (GCD) measurements, and electrochemical impedance spectroscopy (EIS). To verify the feasibility of the prepared composite electrodes for use as flexible supercapacitor, a flexible solid-state supercapacitor was assembled by two identical composite electrodes of CNFs-loaded GO/PEDOT-lCNTs, with the PVA/H_3PO_4 gel as solid electrolyte. The capacitive performances and cycle stability of this highly flexible supercapacitor were tested, which successfully lighted a light-emitting diode (LED). This result is anticipated to stimulate practical applications.

2. Experimental

2.1. Materials

Natural graphite powder (325 mesh) was purchased from Guangfu Research Institute (Tianjin, China). Short and long carboxylated multi-wall carbon nanotubes (sCNTs-COOH and lCNTs-COOH) were obtained from Chengdu Organic Chemicals Co., Ltd., which were made by chemical vapor deposition (CVD) method, and their length was 0.5—2 and 10—30 μm, respectively. Carbon nanotubes thin films (CNFs, thickness of 20 μm) were supplied by Hengqiu Tech. Inc. (Soochow, China). 3, 4-ethylenedioxythiophene (EDOT, Ourchem®, 99%) and polyvinyl alcohol (PVA)-124 were purchased from Sinopharm (Shanghai, China).

2.2. Preparation of the electrode and supercapacitor

Graphite oxide was prepared from natural graphite powder with the modified Hummers method [32,33], and GO was obtained by subsequent exfoliation by ultrasonication. The flexible ternary composite electrodes of CNFs-loaded GO supported poly(3,4-ethylenedioxythiophene)-CNTs (GO/PEDOT-CNTs) were fabricated through a facile electrochemical codeposition method. The aqueous deposition bath containing 0.01 M EDOT monomer, 1 mg mL^{-1} GO, and 1 mg mL^{-1} sCNTs-COOH or lCNTs-COOH was dispersed adequately under ultrasonication for about 15 min. After that, the electrodeposition was performed with a three-electrode system, in which CNFs with 0.5 cm × 1 cm conductive areas serve as the working electrode, large areal Pt sheet acts as the counter electrode and saturated calomel electrode (SCE) as the reference electrode. A

galvanostatic mode with a current density of 1 mA cm^{-2} was used for 30 min, during which the composite films grew on the CNFs with a total charge of 1.8 C cm^{-2} passed. Subsequently, the CNFs-loaded composite electrodes were rinsed with deionized water to remove the unreacted substance. The flexible composite electrodes obtained with short and long CNTs were termed as GO/PEDOT-sCNTs and GO/PEDOT-lCNTs, respectively. As a comparison, the GO/PEDOT electrodes were prepared with the same electrodeposition procedure, just without CNTs-COOH in the deposition bath. The mass of composites was measured by weighing discrepancy of the CNFs before and after electrodeposition using a MS105DU Mettler-Toledo microbalance with an accuracy of 10 μg, and the mass reported is the average value of 3 parallel samples.

The flexible solid-state supercapacitors were fabricated by assembling two pieces of identical CNFs-loaded composites electrodes with a sandwiched separator (a filter paper with thickness of 20 μm) and PVA/H$_3$PO$_4$ gel as the solid electrolyte. After that, the devices were placed in the air at room temperature to vaporize the excess water. PVA/H$_3$PO$_4$ gel electrolyte was prepared as follows: 1 g H$_3$PO$_4$ was mixed with 10 mL deionized water, and then 1 g PVA powder was added. The mixture was heated to 85 °C under vigorous stirring until the solution became clear. The gel electrolyte was obtained after cooling the solution down.

2.3. Characterizations

A Bruker Tensor 27 FT-IR Spectrometer was used to obtain the FT-IR spectra, and the samples tested were prepared by potassium bromide tabletting. The X-ray diffraction (XRD) patterns were recorded on a Rigaku Ultima IV X-ray diffractometer. The morphology of the composites prepared was observed using a field emission scan electron microscope (SEM, JSM-6701F, JEOL) operated with a voltage of 10.0 kV, and a high resolution transmission electron microscopy (TEM, JEM-2100, JEOL) operating at 200 kV. For the FT-IR and TEM characterizations, the samples were scraped from the films-deposited conducting glasses, because it is difficult to scrape from the surface of the films deposited CNFs.

All the electrochemical behaviors including the cyclic voltammograms (CV), galvanostatic charge-discharge (GCD) curves and the electrochemical impedance spectra (EIS) were measured using an electrochemical workstation (CHI 660E, Chenhua, China) in 1.0 M KCl aqueous solution with three-electrode system, in which a saturated calomel electrode (SCE) serves as reference electrode and a large area Pt foil as the counter electrode. The electrochemical behaviors were characterized between potentials of −0.4–0.6 V vs. SCE. EIS was recorded in the frequency range from 0.01 to 10^5 Hz with a 5 mV amplitude referring to the open circuit potential.

3. Results and discussion

3.1. Compositions and structures

As shown in Fig. 1, in the process of electrodeposition to form the ternary composites of GO/PEDOT-CNTs, oxidative polymerization of the EDOT monomer takes place, during which the anionic GO and carboxylated CNTs act simultaneously as the charge carriers in deposition bath, as well as the counter ions for charge balancing of PEDOT. Fig. 2a shows the FT-IR spectra of sCNTs-COOH, lCNTs-COOH, GO, PEDOT, GO/PEDOT-sCNTs, and GO/PEDOT-lCNTs. The peak located at 1722 cm^{-1} in the sCNT-COOH and lCNT-COOH spectra originates from the C=O stretching vibration of the carboxyl [34]. For the spectrum of GO, the peak at 1703 cm^{-1} can also be attributed to the C=O stretching of carbonyl. The peaks located at 1413 and 1235 cm^{-1} are ascribed to the O−H deformation and C−OH stretching vibration, and the peak at 1055 cm^{-1} is the

characteristic peak of the epoxide group [35]. In the pure PEDOT spectrum, the vibration modes of the C−S bond in the thiophene ring are located at 692, 841, and 980 cm^{-1}, the peak at 926 cm^{-1} is related to the deformation mode of ethylenedioxy ring [36–38], and the vibrations at 1058, 1089, 1144, and 1203 cm^{-1} are due to the stretching of the C−O−C bond in the ethylenedioxy group [36]. In addition, the quinoid structure and stretching modes of C−C and C=C in the thiophene ring result in the vibrations at around 1350 and 1518 cm^{-1}, respectively [39].

Comparing to that of PEDOT, the FT-IR spectra of both GO/PEDOT-sCNTs and GO/PEDOT-lCNTs exhibit all the characteristic peaks of PEDOT. The only difference is that the vibration band originating from C−C stretching in the thiophene ring of GO/PEDOT-sCNTs and GO/PEDOT-lCNTs has a redshift from 1350 to 1330 cm^{-1}. This redshift is ascribed to the electrostatic interaction between the PEDOT cations and anionic CNTs, as well as the π−π interactions and hydrogen bonding between the GO layers and thiophene rings. It should be noted that IR bands associated with GO and CNTs are scarcely detectable, which is probably because their IR intensities are too weak relative to those of PEDOT and thus overlapped with the latter bands. Overall, the FT-IR spectra confirm the formation of the GO/PEDOT-sCNTs and GO/PEDOT-lCNTs composites.

The composites prepared were further characterized by XRD. Fig. 2b shows the XRD patterns of GO, sCNTs-COOH, lCNTs-COOH, PEDOT, GO/PEDOT-sCNTs, and GO/PEDOT-lCNTs. The GO pattern reveals a sharp peak situating at 2θ = 10.9° (002 plane of the hexagonal graphite structure), which corresponds to an interlayer spacing of 0.81 nm of the GO sheets as calculated by the Bragg equation. This value is larger than 0.335 nm of pristine graphite (2θ = 26.6°), due to the introduction of oxygen-containing groups and intercalated water molecules between layers [25]. The broad peak at 21.4° is caused by some aggregations of the GO sheets [40]. The XRD patterns of sCNTs-COOH and lCNTs-COOH show the presence of two peaks at 2θ = 26.0° and 42.9°, corresponding to the 002 and 100 planes of the hexagonal graphite structure [41,42], respectively. The PEDOT pattern exhibits a broad diffraction peak at 2θ = 26°, which is indicative of the amorphous nature of PEDOT [43]. For GO/PEDOT-sCNTs and GO/PEDOT-lCNTs, the XRD patterns show only the broad diffraction peak of PEDOT, located at around 26°. Thereinto, the peak attributed to GO disappears within the composites, manifesting that the PEDOT coatings between the GO nanosheets increase the interlayer spacing of the layered GO [25]. The disappeared XRD peaks of CNTs in the composites is probably ascribed to the overlap and weakening of the PEDOT coatings on the surface of CNTs.

3.2. Morphology

The microstructures of electrode materials are critical for supercapacitors, which influence their electrochemical performance. Fig. 3a exhibits the SEM images of the GO/PEDOT, GO/PEDOT-sCNTs, and GO/PEDOT-lCNTs composites. The images of GO/PEDOT show the microstructures of two-dimensional nanosheets interconnecting with each other, and the curly sheet-like morphology of GO is observed clearly, indicating that GO dominates the composites.

Comparing with those of GO/PEDOT, the images of GO/PEDOT-sCNTs and GO/PEDOT-lCNTs composites display a very different morphology due to the incorporation of CNTs. Notably, the curly sheet-like morphology of GO largely disappears, which is caused by a large amount of PEDOT coatings on the GO and covering its morphology. This observation indicates that the incorporation of CNTs enhances the polymerization of PEDOT, which should contribute to the enlargement of faradaic pseudocapacitance of the
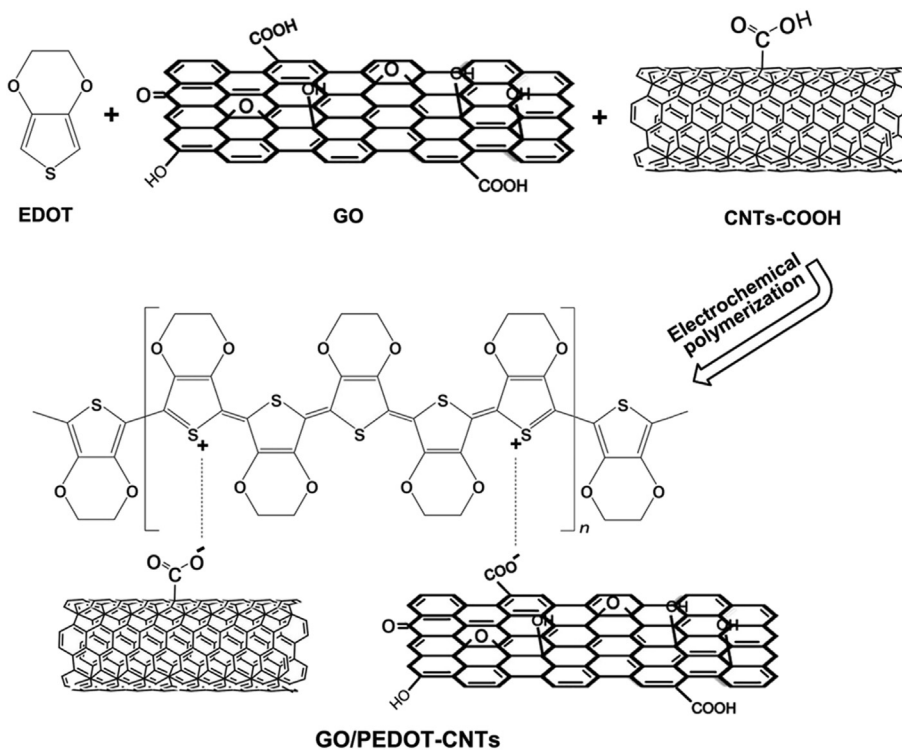
Fig. 1. Schematic diagram of the electrochemical polymerization reaction to prepare the ternary composites of GO/PEDOT-CNTs from EDOT, GO, and CNTs-COOH.
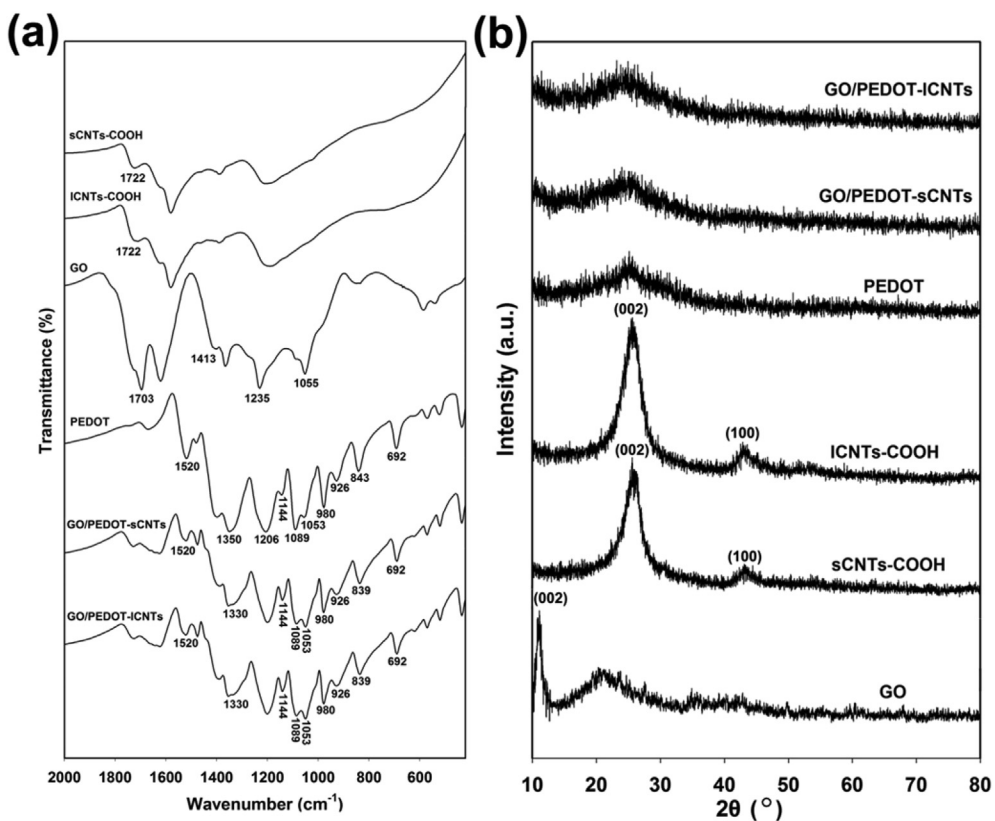
Fig. 2. FT-IR spectra (a) and XRD patterns (b) of sCNTs-COOH, lCNTs-COOH, GO, PEDOT, and the GO/PEDOT-sCNTs and GO/PEDOT-lCNTs composites.
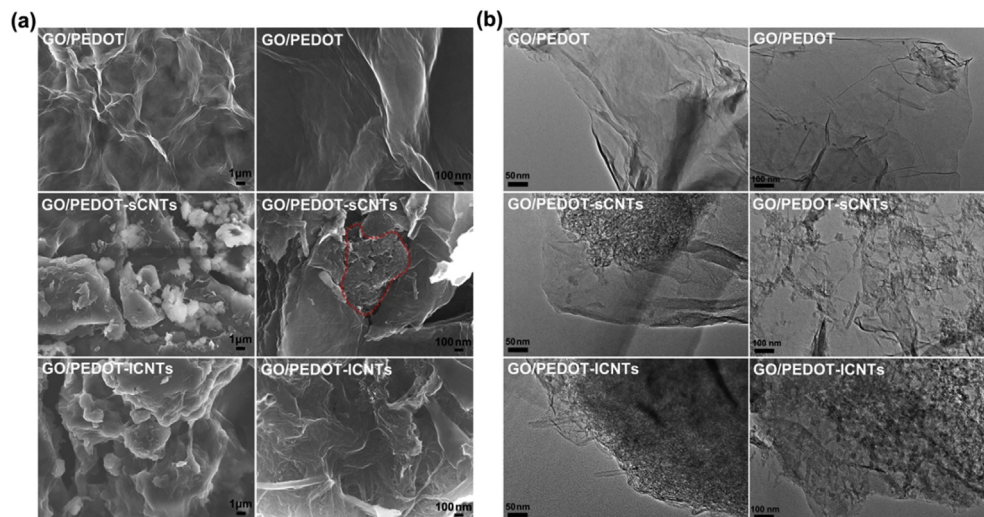
Fig. 3. SEM images (a) at low (left) and high (right) magnification and TEM images (b) at different magnification for the GO/PEDOT, GO/PEDOT-sCNTs, and GO/PEDOT-lCNTs composite electrodes.

composites. A careful observation of the two types of CNTs-incorporated composites suggests the GO/PEDOT-lCNTs composites have more loose and porous microstructures, these should facilitate ion diffusion from electrolyte within the composite films. Furthermore, it can be seen from the SEM images at high magnification that only a bundle of isolated PEDOT-coated CNTs appear in the GO/PEDOT-sCNTs composites (marked with red, dashed line), and the rest of composites is occupied by the PEDOT-coated GO. In contrast, plenty of CNTs are introduced into the GO/PEDOT-lCNTs composites, in which the abundant anionic CNTs may help make the composites less compact, resulting in loose and porous microstructures. It can also be seen that the PEDOT-coated CNTs are relatively uniformly distributed within the composites. These CNTs form an interconnected nano-network, which can effectively promote the charge transfer of the composite films owing to the high conductivity of CNTs.

The observation with SEM is further confirmed by the TEM characterization. Fig. 3b shows that GO is covered by PEDOT-coated CNTs for the two types of CNTs-incorporated composites, which indicates that GO not only acts as the counter-ion, but also as the substrate to support the PEDOT-coated CNTs during the electrochemical codeposition. However, the TEM images of GO/PEDOT-sCNTs show that only part of GO is covered, whereas the whole surface of GO is covered by the PEDOT-coated CNTs for GO/PEDOT-lCNTs, which are well in line with the observation by SEM.

The above morphology characterization indicates that more CNTs were incorporated into the GO/PEDOT-lCNTs composites, and these long CNTs are uniformly distributed, as well as form a conductive interconnected nano-network within the composite films. The optimized composition and special microstructures are beneficial to promote the charge transfer and ion diffusion within the composite films. In the ternary composites of GO/PEDOT-CNTs, PEDOT can contribute high Faradaic pseudocapacitance, GO sheets and CNTs with large surface area provide the large electric double layer capacitance, and the introduced CNTs with high conductivity can make up the disadvantage of insulating GO for high-efficiency charge transfer.

3.3. Electrochemical measurements

The electrochemical behaviors of the as-prepared GO/PEDOT, GO/PEDOT-sCNTs, and GO/PEDOT-lCNTs composite electrodes were initially evaluated using the CV measurements under a three-electrode system in 1 M KCl aqueous solution. As shown in Fig. 4a, all CV curves are close to rectangular in shape at 10 mV s^{-1}, indicative of a highly capacitive nature with superior ion response. In Fig. 4b, with the increase of scan rate, the CV curves still maintain a superior symmetry and display a pair of broad redox peak at $\pm$ 0.2 V, which is related to the doping/dedoping of counter-ions for PEDOT.

For the purpose of applications in small scale electronics and stationary energy storage devices, areal capacitance is a better indicator for supercapacitor performance than gravimetric specific capacitance. Moreover, since the electrode materials are loaded on the substrate by electrodeposition, they are too light to be weighted accurately, so the specific capacitance of electrodes was evaluated in area units in this study. The areal specific capacitance (Cs) of electrodes can be obtained from the CV curves according to the following Eq. (1) [44]:

$$C_S = \left(\frac{1}{2}\int i dV\right)/(S \times \Delta V \times v) \tag{1}$$

where C_s represents the areal specific capacitance (F cm^{-2}), $\int i dV$ the integrated area for the CV curve, S the surface area of active materials (0.5 cm^2 in this study), ΔV the scanning potential window in V, and v the scan rate (V s^{-1}). The CV curves consist of oxidation and reduction curves corresponding to the charge/discharge processes. Thus the integrated area of the nearly symmetrical CV curves multiplied by 1/2 is used to calculate the specific capacitance.

As shown in Fig. 4c, comparing with the GO/PEDOT electrodes, the GO/PEDOT-sCNTs and GO/PEDOT-lCNTs electrodes deliver the larger areal capacitance at all scan rates, suggesting that the incorporation of CNTs with high conductivity effectively promotes the capacitive properties of GO/PEDOT. It can be also seen that the GO/PEDOT-lCNTs electrodes show higher specific capacitance than the GO/PEDOT-sCNTs electrodes at all the CV scan rates. The areal capacitance of GO/PEDOT-sCNTs electrodes is 86.1 mF cm^{-2} at 10 mV s^{-1}. That of GO/PEDOT-lCNTs electrodes is increased to 95.2 mF cm^{-2} at 10 mV s^{-1}, which is higher than the various supercapacitor materials reported, such as active carbon cloth (88 mF cm^{-2} at 10 mV s^{-1}) [45], TiO$_2$@PPy nanowires (64.6 mF cm^{-2} at 10 mV s^{-1}) [46], and CNT/TiO$_2$/ionomer
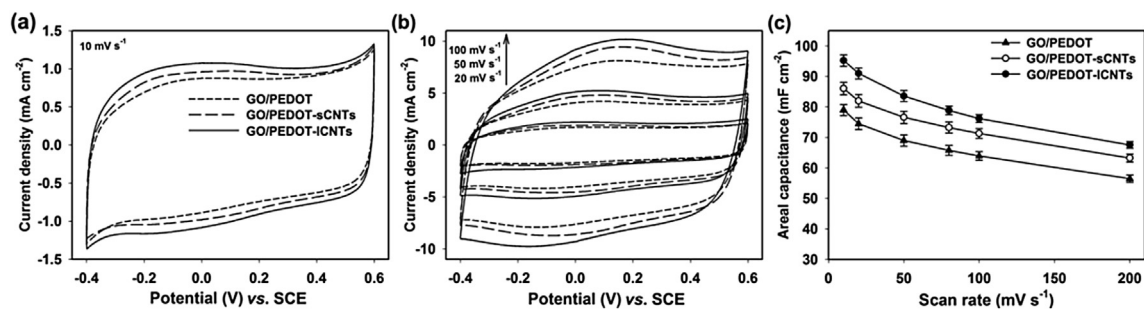
Fig. 4. Cyclic voltammograms at the scan rates of 10 mV s^{-1} (a), 20–100 mV s^{-1} (b), and relationship of areal capacitance with CV scan rate (c) for the CNFs-loaded GO/PEDOT, GO/PEDOT-sCNTs, and GO/PEDOT-lCNTs composite electrodes, tested in 1 M KCl aqueous solution with a three-electrode system. Data in (c) are shown as the mean ± standard error (SE) for the electrodes (n = 3 for each type).

(88 mF cm^{-2} at 5 mV s^{-1}) [47], and PANI/graphite oxide composites (25 mF cm^{-2} at 5 mV s^{-1}) [48]. In addition, when the scan rate increases to 200 mV s^{-1}, the GO/PEDOT-lCNTs electrodes still maintain a high areal capacitance of 67.6 mF cm^{-2}, which indicates a good rate capability. The mass of the GO/PEDOT, GO/PEDOT-sCNTs, and GO/PEDOT-lCNTs composites is 0.75, 0.64, and 0.52 mg, respectively. The gravimetric specific capacitance can be calculated by Eq. (1), in which the surface area (S) is replaced with mass (m). GO/PEDOT, GO/PEDOT-sCNTs, and GO/PEDOT-lCNTs show the specific capacitance of 52.7, 67.2, and 91.6 F g^{-1} at 10 mV s^{-1}, respectively. In short, the results of CV measurements reveal that the long CNTs can more effectively boost the capacitive performance of the GO/PEDOT-CNTs composites.

The GCD tests were also performed to further compare the capacitive performance of the two types of GO/PEDOT-CNTs electrodes. Fig. 5a illustrates the GCD curves for the GO/PEDOT-sCNTs and GO/PEDOT-lCNTs electrodes at different current densities. All the charging curves are symmetric with respect to their discharge counterparts. The curves also show good linear potential-time profiles, indicating the ideal capacitive behavior and fast Faraday redox reaction of the composites. Based on the GCD curves, the areal specific capacitance of electrodes can be given with the following equation:

$$C_S = (i \times t)/(S \times \Delta V) \qquad (2)$$

where C_s is the areal specific capacitance (F cm^{-2}), i the discharge current (A), t the discharge time (s), S the surface area of the active substance (0.5 cm^2 in this research), and ΔV the discharging potential window (V). It can be seen from Fig. 5b that the GO/PEDOT-lCNTs electrodes display the higher specific capacitance at all GCD current densities. Thereinto, the GO/PEDOT-sCNTs electrodes present a specific capacitance of 89.1 mF cm^{-2} at 0.5 mA cm^{-2}, while

that of GO/PEDOT-lCNTs electrodes reaches 100.3 mF cm^{-2} at 0.5 mA cm^{-2}, which are comparable to those of the previous electrode materials such as 3D porous graphene/polyaniline composites (67.2 mF cm^{-2} at 0.05 mA cm^{-2}) and Fe$_3$O$_4$@SnO$_2$ core-shell nanorod array (7.013 mF cm^{-2} at 0.2 mA cm^{-2}) [49,50]. As much as 75.1% and 76.8% of initial capacitance can be maintained even when the GCD current density increases by 20 times (75.0 and 69.0 mF cm^{-2} at 10 mA cm^{-2}) for the GO/PEDOT-lCNTs and GO/PEDOT-sCNTs electrodes, respectively, demonstrating superior rate performance. The GO/PEDOT-sCNTs electrodes show slightly better capacitance retention, which can probably be attributed to the fact that the film of GO/PEDOT-sCNTs (9.5 μm) is slightly thinner than that of GO/PEDOT-lCNTs (10 μm), resulting in slightly shorter transmission distance between electron and current collector. The aforementioned results from GCD tests are in accord with those of the CV measurements.

The EIS tests were carried out to evaluate the charge transfer and electrolyte ion diffusion in the electrode/electrolyte interface, and the obtained EIS complex plane plots are shown in Fig. 5c. A feature of vertical trend for impedance plots at low frequencies can be observed for the two types of electrodes, manifesting the capacitive character [51]. Comparing with the GO/PEDOT-sCNTs electrodes, the straight line in the low frequency region for the GO/PEDOT-lCNTs electrodes leans more towards the imaginary axis, indicative of the better capacitive behavior. The fact that a semicircle at high frequency is not found for the two types of electrodes, in the inset of Fig. 5c, is attributed to the low interfacial charge-transfer resistance [39]. Also observed in the inset of Fig. 5c is that the intercept at x-axis for the GO/PEDOT-lCNTs electrodes is smaller than that of the GO/PEDOT-sCNTs electrodes, suggesting a smaller equivalent series resistance (ESR). ESR is related to the electrolyte solution resistance, the intrinsic resistance of active materials, and the interfacial contact resistance between current
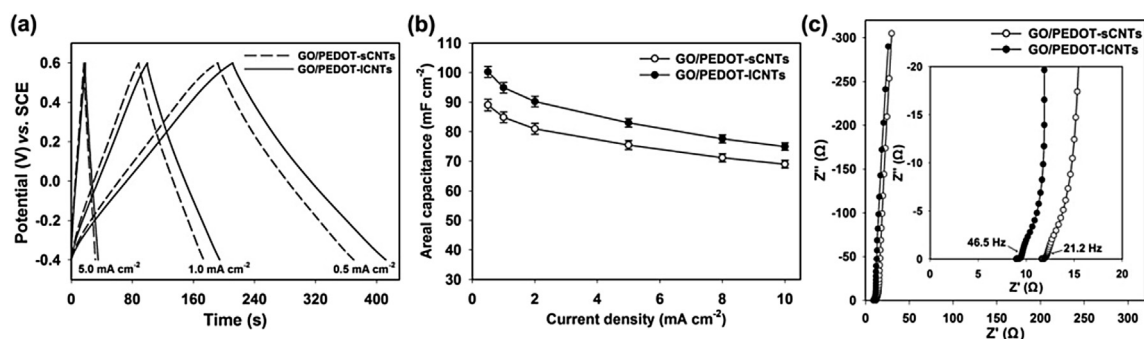
Fig. 5. GCD curves at various current densities (a), areal capacitance vs. GCD current density (b), and EIS complex plane plots (c) for the CNFs-loaded GO/PEDOT-sCNTs and GO/PEDOT-lCNTs composite electrodes. The inset in (c) is the EIS plots in the high-frequency region. Data in (b) are presented as the mean ± standard error (SE) for the electrodes (n = 3 for each type).

collectors and active materials [52]. Furthermore, the transition point between the 45° region and the vertical line in the low-frequency region is called the "knee frequency", beyond which the capacitive behavior is replaced by the more inclined diffusion line. Higher knee frequency means faster charge transfer rates and lower diffusion impedance [53]. The GO/PEDOT-lCNTs electrodes exhibit a higher knee frequency (46.5 Hz) than the GO/PEDOT-sCNTs electrodes (21.2 Hz), as obtained from the inset of Fig. 5c. The EIS tests further indicate that the GO/PEDOT-lCNTs electrodes have better charge transfer and ion diffusion of electrolyte, which consequently result in the higher specific capacitance and excellent rate performance.

As observed from the SEM and TEM images, in comparison with the short CNTs-incorporated GO/PEDOT-sCNTs electrodes, the long CNTs-incorporated GO/PEDOT-lCNTs electrodes have superior electrochemical behaviors due to its composition and specific microstructures. Plenty of CNTs are introduced into the GO/PEDOT-lCNTs composites, resulting in loose and porous microstructures. The hydrophilic GO sheets as the substrate offer high electrochemical surface area for the electrical double-layer. Meanwhile, the supported PEDOT-coated CNTs are relatively uniformly distributed in the composites, and the conductive interconnected nano-network can significantly promote the charge transfer.

3.4. Supercapacitor tests

In practical applications, flexible electronic devices desire power sources with high flexibility, stability, and environmental friendliness. To verify the feasibility of the prepared composite electrodes for utilization as flexible supercapacitor, a solid-state supercapacitor was assembled by two identical CNFs-loaded GO/PEDOT-lCNTs composite electrodes with PVA/H_3PO_4 gel as the solid electrolyte. Fig. 6 shows the CV and GCD curves of the assembled flexible supercapacitor device, as well as its areal specific capacitance obtained from the corresponding CV and GCD curves. The

specific capacitance of the device is calculated according to the Eq. (1) and Eq. (2), respectively.

It can be seen from Fig. 6a that the CV curves maintain the rectangular shape with almost symmetric i-E response at all scan rates ranging from 10 to 100 mV s^{-1}, and the current shows obvious increase with the scan rate. The device achieves the specific capacitance of 33.4 mF cm^{-2} at 10 mV s^{-1}. In addition, with the increase of CV scan rate, the capacitance shows a relatively smooth decline (Fig. 6b), demonstrating its superior rate performance. Likewise, all the GCD curves (Fig. 6c) of the device have symmetric, triangular shape and linear potential-time relationship, with a high specific capacitance of 32.3 mF cm^{-2} at 0.5 mA cm^{-2}. It is comparable to other solid-state supercapacitors in the literature, such as graphene/polyaniline composite based supercapacitors (23 mF cm^{-2} at 0.1 mA cm^{-2}) and cellulose nanofibers/[PANi-PEDOT] based supercapacitors (4.22 mF cm^{-2} at 0.0043 mA cm^{-2}) [54,55]. Furthermore, with the increase of current densities, the capacitance also shows a relatively smooth decline (Fig. 6d). The specific capacitance maintains 58% of initial value when the current density increases by as much as 20 times (18.7 mF cm^{-2} at 10 mA cm^{-2}), indicating that the flexible solid-state supercapacitor has ideal electrochemical capacitive properties.

According to the GCD curves, the areal specific energy density and power density of the assembled supercapacitor can be further calculated by the Eqs. (3) and (4) [25,48], respectively.

$$E = \frac{\frac{1}{2}C_S\Delta V^2}{3600} \tag{3}$$

$$P = \frac{3600E}{t} \tag{4}$$

where E is the areal specific energy density (Wh cm^{-2}), P the areal specific power density (W cm^{-2}), C_S the areal specific capacitance (F
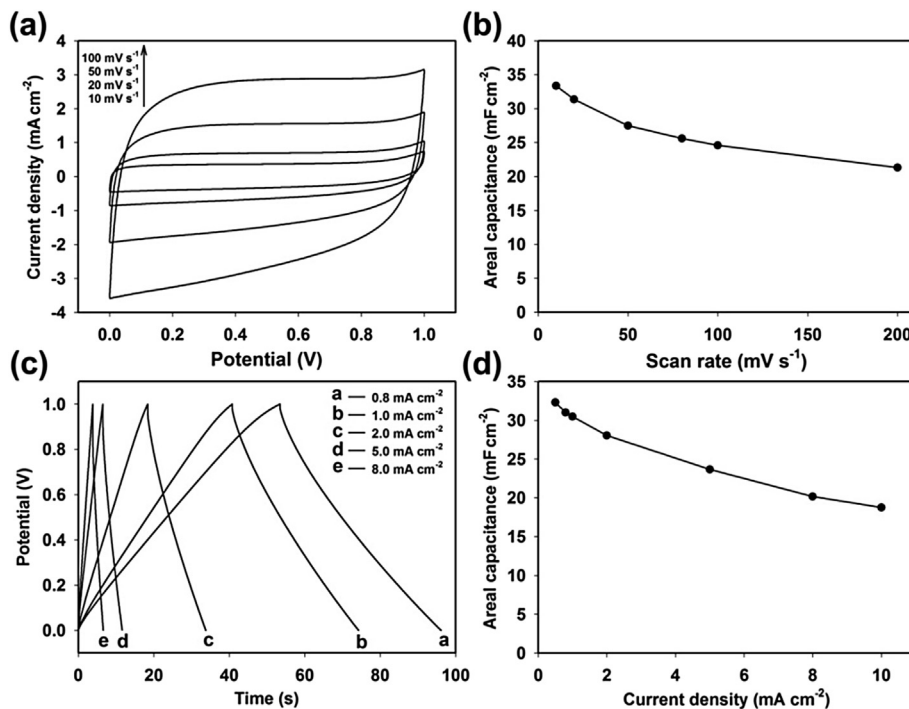
Fig. 6. CV curves at varying scan rates (a), areal capacitance *vs.* CV scan rate (b), GCD curves at various current densities (c), and areal capacitance *vs.* GCD current density (d) of the flexible solid-state supercapacitor assembled by two identical CNF-loaded GO/PEDOT-lCNTs composite electrodes with PVA/H_3PO_4 gel as a solid electrolyte.

cm^{-2}) obtained by Eq. (2), ΔV the potential window subtracting iR drop (V), t the discharge time (s), and 3600 is for unit conversion between second and hour. The Ragone plot in Fig. 7a shows the high power-energy character of the supercapacitor, with the highest power density of 4.0 mW cm^{-2} and the maximum energy density of 4.4 μWh cm^{-2} being achieved. Long cycle life is a crucial parameter for practical applications of supercapacitor, Fig. 7b presents the cycle stability of the supercapacitor device, which underwent 5000 CV cycles at 50 mV s^{-1} in tests. The result indicates that no decline occurs for the first 2800 cycles, and 97.5% of initial capacitance maintains after 5000 cycles, demonstrating its excellent long-term cycle stability.

For the purpose of applications for integrated energy devices, the supercapacitors should exhibit high flexibility without adverse on the device performance. As shown in Fig. 8a, the as-prepared supercapacitor is highly flexible and it can endure the folded, twisted, and rolled states without destroying its construction. Importantly, the electrochemical performances of the device retain nearly unchanged under these states (Fig. 8b). The obtained device is so thin and lightweight that the thickness and weight of the whole device (including the electrodes, electrolyte, and separator) are only around 120 μm and 12.8 mg, respectively, and yet it can deliver the volumetric specific capacitance of 2.7 F cm^{-3} at 0.042 A cm^{-3}, which is higher than those of other solid-state supercapacitors reported, such as graphene based supercapacitors of 0.45 F cm^{-3} [56], carbon fiber/MnO_2 based supercapacitors of 2.5 F/cm^{-3} [57], and H$-$$TiO_2$ based asymmetric supercapacitors of 0.7 F cm^{-3} [58]. These features enable the entire device to be thinner and more flexible, making the design of compact and light devices possible. To simulate practical applications, three supercapacitor units were connected in series to light up a light-emitting diode (LED) (Fig. 8c) after charging, which demonstrates its practical use, suggesting its great potential for flexible and lightweight electronics in energy management applications.

It should be pointed out that nanomaterials have potential adverse environmental impact for their tiny size. However, the electrode materials being reported herein are composite materials, featuring integration and large size. Thus they differ essentially from individual nanomaterials like CNTs. In addition, the economic viability is an important factor to affect the practical application of electrode materials. Although CNTs and CNFs are relatively costly materials, currently they have become very cheap compared to the
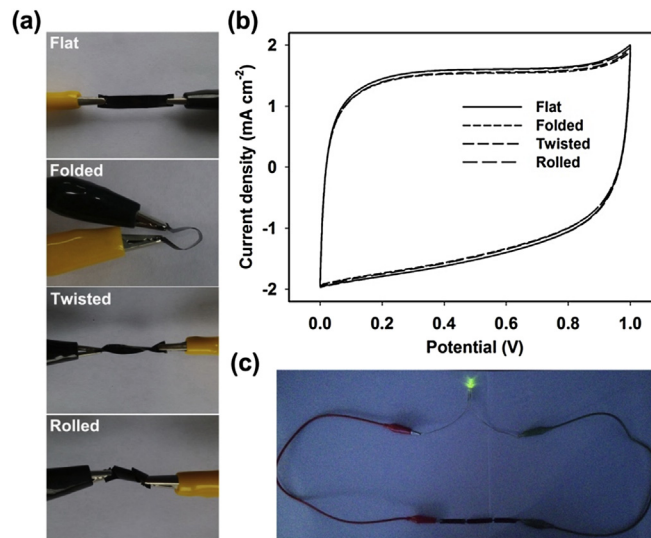
Fig. 8. (a) Optical photographs of the flexible solid-state supercapacitor with four different states: flat, folded, twisted, and rolled; (b) CV curves at 50 mV s^{-1} scan rate for supercapacitor under four different states; (c) Photograph of a green light-emitting diode (LED) being lit by a device composed of three supercapacitors connected in series. (For interpretation of the references to color in this figure legend, the reader is referred to the web version of this article.)

days when they first appeared, and their preparation cost is getting lower and lower with the development of fabrication technology. So CNTs and CNFs have great potential for supercapacitor applications due to their superior conductivity and flexibility.

4. Conclusions

In summary, we have prepared CNFs-loaded ternary composite electrodes with GO supported PEDOT-CNTs hybrid structure, via a facile electrochemical codeposition method. Electrochemical measurements indicate that the long CNTs-incorporated GO/PEDOT-lCNTs electrodes have superior capacitive performances with respect to the short CNTs-incorporated GO/PEDOT-lCNTs electrodes, which can be attributed to the optimal composition and specific microstructures of the former. Furthermore, a highly flexible solid-state supercapacitor based on the CNFs-loaded GO/PEDOT-lCNTs composites has been fabricated, and the device shows the ultrathin, lightweight, and highly flexible features, which has a high specific capacitance and excellent cycle stability. The superior performances and the ease of fabrication suggest that the supercapacitor fabricated is a good candidate for highly flexible and lightweight integrated electronics.

Acknowledgements

References

[1] D.S. Yu, K. Goh, H. Wang, L. Wei, W.C. Jiang, Q. Zhang, L.M. Dai, Y. Chen, Nat. Nanotechnol. 9 (2014) 555–562.
[2] Z.Y. Xiong, C.L. Liao, W.H. Han, X.G. Wang, Adv. Mater. 27 (2015) 4469–4475.
[3] W. Wang, W.Y. Liu, Y.X. Zeng, Y. Han, M.H. Yu, X.H. Lu, Y.X. Tong, Adv. Mater 27 (2015) 3572–3578.
[4] X.L. Wang, G.Q. Shi, Energy Environ. Sci. 8 (2015) 790–823.
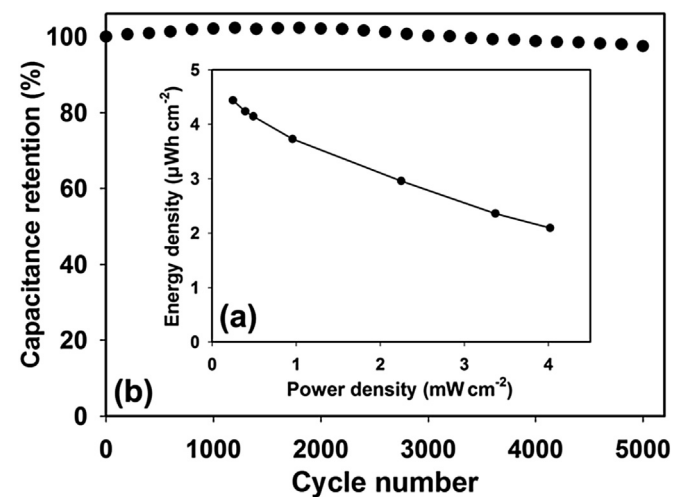
Fig. 7. Ragone plots (a) and the relationship of specific capacitance retention rate and cycle number (b) for the solid-state supercapacitor assembled by two identical CNFs-loaded GO/PEDOT-lCNTs composite electrodes.

[5] Q.L. Zhou, X.K. Ye, Z.Q. Wan, C.Y. Jia, J. Power Sources 296 (2015) 186–196.
[6] Y.B. Xie, C. Xia, H.X. Du, W. Wang, J. Power Sources 286 (2015) 561–570.
[7] Y. Liu, B. Weng, J.M. Razal, Q. Xu, C. Zhao, Y. Hou, S. Seyedin, R. Jalili, G.G. Wallace, J. Chen, Sci. Rep. 5 (2015) 17045.
[8] P.Y. Tang, L.J. Han, L. Zhang, ACS Appl. Mater. Interface 6 (2014) 10506–10515.
[9] Y. Hu, H.H. Cheng, F. Zhao, N. Chen, L. Jiang, Z.H. Feng, L.T. Qu, Nanoscale 6 (2014) 6448–6451.
[10] W.Q. Ma, H.H. Nan, Z.X. Gu, B.Y. Geng, X.J. Zhang, J. Mater. Chem. A 3 (2015) 5442–5448.
[11] J.M. Griffin, A.C. Forse, W.Y. Tsai, P.L. Taberna, P. Simon, C.P. Grey, Nat. Mater. 14 (2015) 812–819.
[12] M.S. Javed, S.G. Dai, M.J. Wang, D.L. Guo, L. Chen, X. Wang, C.G. Hu, Y. Xi, J. Power Sources 285 (2015) 63–69.
[13] L.Y. Yuan, B. Yao, B. Hu, K.F. Huo, W. Chen, J. Zhou, Energy Environ. Sci. 6 (2013) 470–476.
[14] P. Simon, Y. Gogotsi, Nat. Mater. 7 (2008) 845–854.
[15] W. Xing, C.C. Huang, S.P. Zhuo, X. Yuan, G.Q. Wang, D. Hulicova-Jurcakova, Z.F. Yan, G.Q. Lu, Carbon 47 (2009) 1715–1722.
[16] H. Jiang, P.S. Lee, C.Z. Li, Energy Environ. Sci. 6 (2013) 41–53.
[17] M.K. Liu, Y.E. Miao, C. Zhang, W.W. Tjiu, Z.B. Yang, H.S. Peng, T.X. Liu, Nanoscale 5 (2013) 7312–7320.
[18] J.W. Zhao, J. Chen, S.M. Xu, M.F. Shao, Q. Zhang, F. Wei, J. Ma, M. Wei, D.G. Evans, X. Duan, Adv. Funct. Mater. 24 (2014) 2938–2946.
[19] J.H. Kim, S. Lee, J. Choi, T. Song, U. Paik, J. Mater. Chem. A 3 (2015) 20459–20464.
[20] Y. Zhao, Y.N. Meng, P. Jiang, J. Power Sources 259 (2014) 219–226.
[21] J.Y. Cao, Y.M. Wang, J.C. Chen, X.H. Li, F.C. Walsh, J.H. Ouyang, D.C. Jia, Y. Zhou, J. Mater. Chem. A 3 (2015) 14445–14457.
[22] W.L. Wu, Y.F. Li, G.H. Zhao, L.Q. Yang, D. Pan, J. Mater. Chem. A 2 (2014) 18058–18069.
[23] J. Li, H.Q. Xie, Y. Li, J. Power Sources 241 (2013) 388–395.
[24] X.L. Li, Q.N. Zhong, X.L. Zhang, T.T. Li, J.M. Huang, Thin Solid Films 584 (2015) 348–352.
[25] H.H. Zhou, G.Y. Han, Y.M. Xiao, Y.Z. Chang, H.J. Zhai, J. Power Sources 263 (2014) 259–267.
[26] S. Iijima, Nature 354 (1991) 56–58.
[27] M.F.L. De Volder, S.H. Tawfick, R.H. Baughman, A.J. Hart, Science 339 (2013) 535–539.
[28] Y.L. Chen, L.H. Du, P.H. Yang, P. Sun, X. Yu, W.J. Mai, J. Power Sources 287 (2015) 68–74.
[29] Y. Zhang, K.S. Suslick, Chem. Mater. 27 (2015) 7559–7563.
[30] C.H. Lei, P. Wilson, C. Lekakou, J. Power Sources 196 (2011) 7823–7827.
[31] S. Zeng, H. Chen, F. Cai, Y. Kang, M. Chen, Q. Li, J. Mater. Chem. A 3 (2015) 23864–23870.
[32] W.S. Hummers, R.E. Offeman, J. Am. Chem. Soc. 80 (1958) 1339.
[33] Y.X. Xu, H. Bai, G.W. Lu, C. Li, G.Q. Shi, J. Am. Chem. Soc. 130 (2008) 5856–5857.
[34] S. Bhandari, M. Deepa, A.K. Srivastava, A.G. Joshi, R. Kant, J. Phys. Chem. B 113 (2009) 9416–9428.
[35] C.Z. Zhu, J.F. Zhai, D. Wen, S.J. Dong, J. Mater. Chem. 22 (2012) 6300–6306.
[36] H.J. Shin, S.S. Jeon, S.S. Im, Synth. Met. 161 (2011) 1284–1288.
[37] L. Chen, C.Z. Yuan, H. Dou, B. Gao, S.Y. Chen, X.G. Zhang, Electrochim. Acta 54 (2009) 2335–2341.
[38] D.X. Han, G.F. Yang, J.X. Song, L. Niu, A. Ivaska, J. Electroanal. Chem. 602 (2007) 24–28.
[39] Y.Q. Han, B. Ding, H. Tong, X.G. Zhang, J. Appl. Polym. Sci. 121 (2011) 892–898.
[40] Y.Z. Chang, G.Y. Han, J.P. Yuan, D.Y. Fu, F.F. Liu, S.D. Li, J. Power Sources 238 (2013) 492–500.
[41] S.Z. Li, Y.B. Gong, Y.C. Yang, C. He, L.L. Hu, L.F. Zhu, L.P. Sun, D. Shu, Chem. Eng. J. 260 (2015) 231–239.
[42] Y.K. Lee, K.J. Lee, D.S. Kim, D.J. Lee, J.Y. Kim, Synth. Met. 160 (2010) 814–818.
[43] G.P. Pandey, A.C. Rastogi, Electrochim. Acta 87 (2013) 158–168.
[44] Y. Zou, Q. Wang, C. Xiang, Z. She, H. Chu, S. Qiu, F. Xu, S. Liu, C. Tang, L. Sun, Electrochim. Acta 188 (2016) 126–134.
[45] G.M. Wang, H.Y. Wang, X.H. Lu, Y.C. Ling, M.H. Yu, T. Zhai, Y.X. Tong, Y. Li, Adv. Mater. 26 (2014) 2676–2682.
[46] M.H. Yu, Y.X. Zeng, C. Zhang, X.H. Lu, C.H. Zeng, C.Z. Yao, Y.Y. Yang, Y.X. Tong, Nanoscale 5 (2013) 10806–10810.
[47] C. Huang, N.P. Young, P.S. Grant, J. Mater. Chem. A 2 (2014) 11022–11028.
[48] H.G. Wei, J.H. Zhu, S.J. Wu, S.Y. Wei, Z.H. Guo, Polymer 54 (2013) 1820–1831.
[49] Q.Q. Zhou, Y.R. Li, L. Huang, C. Li, G.Q. Shi, J. Mater. Chem. A 2 (2014) 17489–17494.
[50] R.Z. Li, X. Ren, F. Zhang, C. Du, J.P. Liu, Chem. Commun. 48 (2012) 5010–5012.
[51] C. Peng, J. Jin, G.Z. Chen, Electrochim. Acta 53 (2007) 525–537.
[52] H.Y. Mi, X.G. Zhang, X.G. Ye, S.D. Yang, J. Power Sources 176 (2008) 403–409.
[53] Y. Song, J.L. Xu, X.X. Liu, J. Power Sources 249 (2014) 48–58.
[54] X.B. Zang, X. Li, M. Zhu, X.M. Li, Z. Zhen, Y.J. He, K.L. Wang, J.Q. Wei, F.Y. Kang, H.W. Zhu, Nanoscale 7 (2015) 7318–7322.
[55] X. Wang, K.Z. Gao, Z.Q. Shao, X.Q. Peng, X. Wu, F.J. Wang, J. Power Sources 249 (2014) 148–155.
[56] M.F. El-Kady, V. Strong, S. Dubin, R.B. Kaner, Science 335 (2012) 1326–1330.
[57] X. Xiao, T.Q. Li, P.H. Yang, Y. Gao, H.Y. Jin, W.J. Ni, W.H. Zhan, X.H. Zhang, Y.Z. Cao, J.W. Zhong, L. Gong, W.C. Yen, W.J. Mai, J. Chen, K.F. Huo, Y.L. Chueh, Z.L. Wang, J. Zhou, ACS Nano 6 (2012) 9200–9206.
[58] X.H. Lu, M.H. Yu, G.M. Wang, T. Zhai, S.L. Xie, Y.C. Ling, Y.X. Tong, Y. Li, Adv. Mater 25 (2013) 267–272.